SPECIAL
DYNAMO/CINDY/AMIE/LASP
COLLECTION

Practical and Intrinsic Predictability of Multiscale Weather and Convectively Coupled Equatorial Waves during the Active Phase of an MJO

YUE YING AND FUQING ZHANG

Department of Meteorology and Atmospheric Science, and Center for Advanced Data Assimilation and Predictability Techniques, The Pennsylvania State University, University Park, Pennsylvania

(Manuscript received 23 May 2017, in final form 28 August 2017)

ABSTRACT

Through a series of convection-permitting regional-scale ensembles based on the Weather Research and Forecasting (WRF) Model, this study investigates the predictability of multiscale weather and convectively coupled equatorial waves during the active phase of a Madden–Julian oscillation (MJO) event over the Indian Ocean from 12 October to 12 November 2011. It is found that the practical predictability limit, estimated by the spread of the ensemble perturbed with realistic initial and boundary uncertainties, is as much as 8 days for horizontal winds, temperature, and humidity for scales larger than 2000 km that include equatorial Rossby, Kelvin, inertia–gravity, and mixed Rossby–gravity waves. The practical predictability limit decreases rapidly as scale decreases, resulting in a predictable time scale less than 1 day for scales smaller than 200 km. Through further experiments using minute initial and boundary perturbations an order of magnitude smaller than the current realistic uncertainties, the intrinsic predictability limit for tropical weather at larger scales (>2000 km) is estimated to be achievable beyond 2 weeks, but the limit is likely still less than 3 days for the small scales (<200 km).

1. Introduction

The tropical atmosphere consists of weather systems spanning a wide range of spatial and temporal scales. At the planetary scale, the Madden–Julian oscillation (MJO) is found to be the dominant mode of intraseasonal variability with typical periods of 20–100 days (Madden and Julian 1971, 1972; Zhang 2005). The active phase of an MJO is characterized by enhanced deep convection and intense precipitation that propagates eastward at a speed around $5\,m\,s^{-1}$. Within the MJO envelope, a wide variety of convectively coupled equatorial waves (CCEWs; Wheeler and Kiladis 1999; Kiladis et al. 2009) reside, including equatorial Rossby, Kelvin, mixed Rossby–gravity (MRG), and inertia–gravity (IG) waves. The equatorial Rossby waves are large-scale "cyclone pairs" that propagate westward at a speed around $4.5\,m\,s^{-1}$ (Kiladis et al. 2009). The equatorial Kelvin waves are also known as the super cloud clusters that propagate eastward at a speed of $15–20\,m\,s^{-1}$ (Nakazawa 1988; Dunkerton and Crum 1995). The MRG waves propagate westward at a speed of $15–20\,m\,s^{-1}$ and have the potential to develop into tropical cyclones (Takayabu and Nitta 1993; Dickinson and Molinari 2002). The westward-propagating IG (WIG) waves have a wide range of spatiotemporal scales, ranging from smaller-scale diurnal to semidiurnal variations to larger-scale 2-day waves (Haertel and Kiladis 2004).

How predictable are the tropical weather systems and CCEWs? The concept of atmospheric predictability can be grossly categorized into intrinsic versus practical predictability (Lorenz 1996; Melhauser and Zhang 2012). Intrinsic predictability refers to the ability to predict given nearly perfect representation of the dynamical system (by a forecast model) and nearly perfect initial/boundary conditions, an inherent limit due to the chaotic nature of the atmosphere (Lorenz 1963, 1969; Zhang et al. 2003, 2007; Sun and Zhang 2016). Practical predictability, sometimes also referred to as the prediction skill, is the ability to predict given realistic uncertainties in both the forecast model and initial and boundary conditions (Lorenz 1982, 1996; Zhang et al. 2002, 2006) that can both be large at present. The limit of practical predictability can potentially be extended through the use of more accurate initial conditions (resulting from better data assimilation methods and/or observations) and/or better forecast models (better model physics, numerics, and/or

Corresponding author: Professor Fuqing Zhang, fzhang@psu.edu

DOI: 10.1175/JAS-D-17-0157.1

resolution). Meanwhile, recent studies suggest the predictability of multiscale midlatitude weather and tropical cyclones can be intrinsically limited because of the chaotic nature of moist convection and the rapid upscale error growth, as shown for winter cyclones (Zhang et al. 2003, 2007; Sun and Zhang 2016), summertime continental mesoscale convective systems (e.g., Bei and Zhang 2007; Melhauser and Zhang 2012; Selz and Craig 2015; Zhang et al. 2016), and hurricanes (e.g., Zhang and Sippel 2009; Tao and Zhang 2015).

To the best of our knowledge, the predictability of multiscale tropical weather beyond tropical cyclones is rather underexplored. Using a then-operational global prediction system under a perfect model assumption, Reynolds and Webster (1994) found that the internal error growth rate in the tropics is several times slower than that in midlatitudes, while the external error growth rate due to model deficiencies is considerably larger. Using a global convection-permitting aquaplanet model configured with different resolutions, Mapes et al. (2008) revealed that predictability of tropical weather can be potentially limited by error growth from midlatitude moist baroclinic systems. Several estimates of MJO predictability have been made from global model simulation (Waliser et al. 2003; Nasuno 2013; Neena et al. 2014a,b). Ling et al. (2014) suggested that MJO predictability may differ greatly when considering global or local scales and during different MJO phases. Such scale dependency also results in a more limited predictability estimated from higher-resolution simulation than coarser-resolution global models (Miyakawa et al. 2014).

In 2011, the Dynamics of the MJO (DYNAMO) field campaign was conducted over the Indian Ocean to gather more observations, to advance physical understanding of MJOs, and ultimately to improve MJO prediction (Zhang et al. 2013; Yoneyama et al. 2013). Two moderate-to-strong MJO events occurred during October and November 2011 and were well observed by the field campaign, as documented in Johnson and Ciesielski (2013). More recently, Wang et al. (2015) conducted a successful simulation of these MJOs using the Weather Research and Forecasting (WRF) Model at the convection-permitting resolution with 9-km grid spacing. They showed that the model is capable of reproducing most of the observed MJO features, including its eastward propagation, dynamical structure, and the overall rainfall pattern and magnitude. Sensitivity experiments with the same regional WRF configuration in Zhang et al. (2017) subsequently demonstrated the crucial importance of the global circumnavigating mode in the MJO initiation and propagation. These results motivate the use of such a model as a proxy of the tropical atmosphere for studying its predictability. To the best of our knowledge, the current study represents the first systematic investigation of both the practical and intrinsic limits of multiscale predictability of tropical weather and CCEWs through a series of unprecedented convection-permitting regional-scale ensemble simulations. The resulting predictability estimates provide a benchmark for the future investigation with improved modeling systems.

The remainder of the paper is laid out as follows. The model configuration and design of ensemble simulation are described in section 2. In section 3, an overview is given for the simulated features of CCEWs. The practical predictability is estimated in section 4, followed by an intrinsic predictability assessment in section 5. In section 6, the error growths are analyzed for CCEWs to illustrate their distinct predictability limits. Section 7 summarizes the findings of this study.

2. Experimental design

a. Model configuration and the control simulation

In this study, the WRF Model, version 3.4.1 (Skamarock et al. 2008), is employed to conduct simulations. The model configuration is similar to that described in section 2a of Wang et al. (2015). The computational domain covers the equatorial Indian Ocean and part of the Maritime Continent (20°S–20°N, 50°–120°E). The model grid is 445 × 778 with 9-km spacing, and it has 45 vertical levels with 9 levels in the lowest 1 km and a model top at 20 hPa. The initial condition (IC) and lateral boundary condition (LBC) are specified by the ERA-Interim data (Dee et al. 2011). The sea surface temperature (SST) for the lower boundary condition is updated every 6 h according to the ERA-Interim data.

The WRF double-moment (WDM) scheme (Lim and Hong 2010) is used to parameterize cloud physics with modifications to the shape parameters and terminal velocity of snow. Both shortwave and longwave radiation are treated with the CAM scheme (Collins et al. 2004). Surface processes are represented with the unified Noah model (Chen and Dudhia 2001) with variable surface skin temperature (Zeng and Beljaars 2005). Sub-grid-scale turbulent eddy mixing is parameterized using the Yonsei University (YSU) PBL scheme (Hong et al. 2006). No cumulus parameterization is used, and organized convective motion is explicitly represented by the 9-km model grid. A control simulation of the MJO active phase is initialized at 0000 UTC 12 October and integrated for 31 days, which ends on 12 November 2011. Section 3 will provide an overview of the simulated period and validation of model simulation with observations.

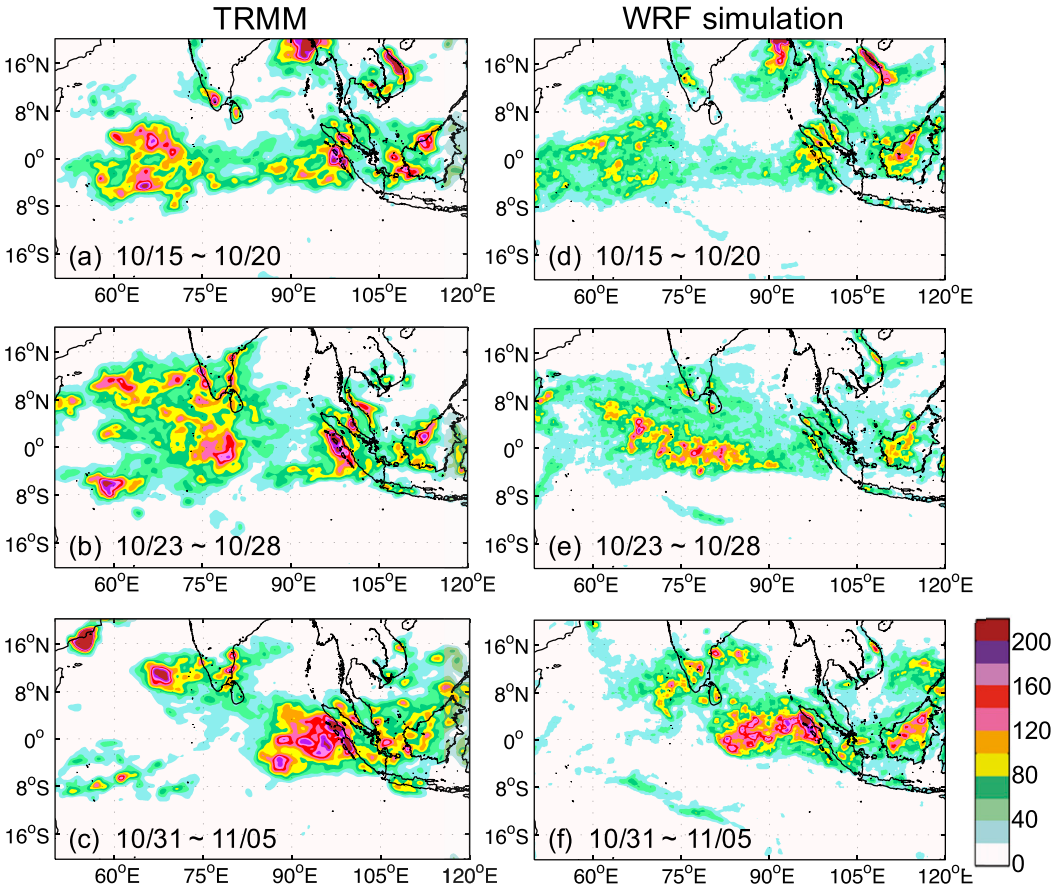

FIG. 1. Horizontal maps of 5-day accumulated precipitation (mm) on (a),(d) 20 Oct, (b),(e) 28 Oct, and (c),(f) 5 Nov. The results are compared between (a)–(c) TRMM observation and (d)–(f) WRF control simulation.

b. *Ensemble simulation*

A pair of 20-member ensembles is conducted to study the practical versus intrinsic predictability of the tropical weather systems and CCEWs. The first ensemble simulation designed to examine the practical predictability limits starts from 18 October to 2 November (corresponding to the MJO phases 1–3). The IC and LBC ensemble perturbations are sampled from the operational European Centre for Medium-Range Weather Forecasts (ECMWF) global ensemble forecasts archived in The Observing System Research and Predictability Experiment (THORPEX) Interactive Grand Global Ensemble (TIGGE).[1] The TIGGE archives 15-day global forecasts of horizontal winds, temperature, geopotential height, and specific humidity at eight pressure levels (1000, 925, 850, 700, 500, 300, 250, and 200 hPa) at 12-h intervals. The then-operational ECMWF ensemble has a horizontal resolution of 32 km (T639) for the first 10 days and 63 km (T319) from day 10 to day 15. Ensemble perturbations from the first 20 TIGGE members are interpolated to the 9-km WRF model grid and to 6-h intervals in time and then are added to the control IC and LBC generated from ERA-Interim data. Since the TIGGE ensemble forecasts are valid at the same time as the IC and LBC being perturbed, the ensemble perturbations are physically consistent with the flow-dependent realistic uncertainties of the unperturbed model atmosphere. With the global model uncertainties downscaled to the regional model at the 9-km resolution, the ensemble forecasts designed herein will provide a realistic estimate of the practical predictability of the tropical weather and CCEWs during the MJO active phase under a perfect model assumption.

The intrinsic predictability is estimated from another set of 20-member ensemble simulations with the IC and LBC perturbation uncertainties reduced to 1% in terms of error energy (or 10% error magnitude) comparing to the ensemble described above, which is a level of

[1] More information on the TIGGE dataset can be found online (https://software.ecmwf.int/wiki/display/TIGGE).

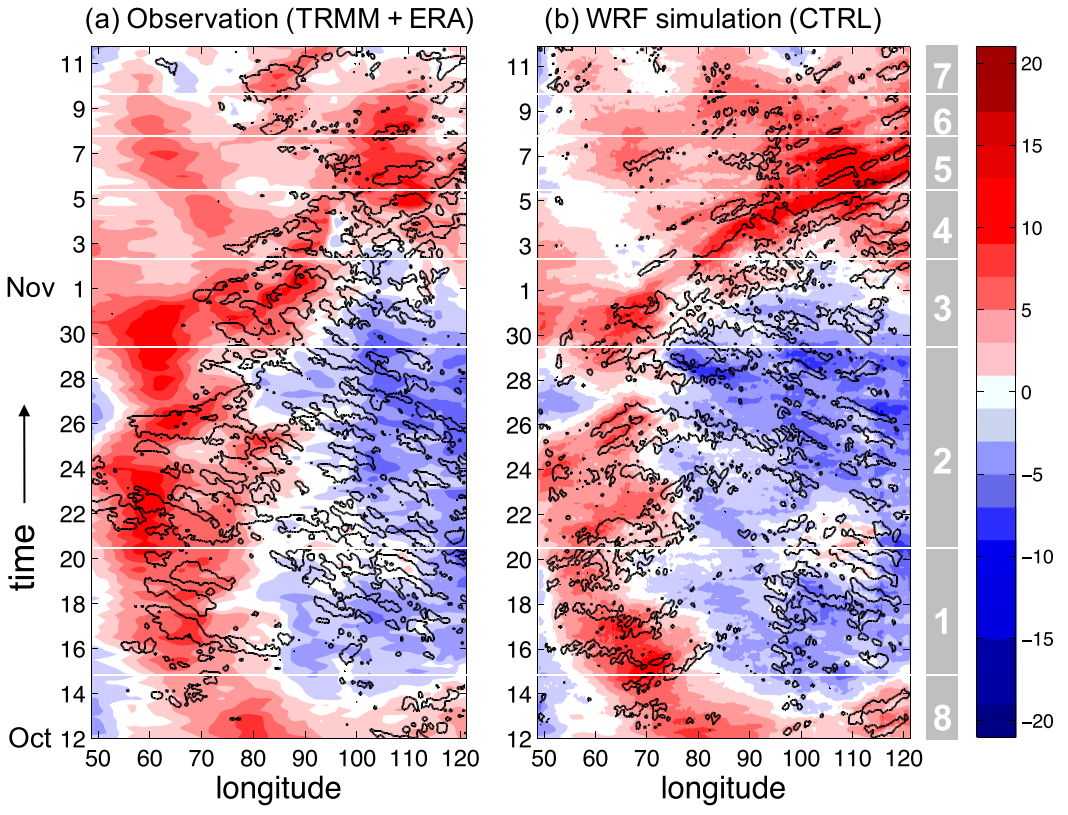

FIG. 2. Longitude–time plots of 850-hPa zonal wind (color shading from −20 to 20 m s^{-1}) and precipitation (black contours of 15 mm day^{-1}) averaged over 5°S–5°N. The results are compared between (a) TRMM precipitation and ERA-Interim zonal wind and (b) WRF control simulation. The white grid and numbers to the right indicate the observed phase of the October 2011 MJO [according to Fig. 6 from Johnson and Ciesielski (2013)]. The precipitation and wind fields are plotted at 3-h intervals, except for ERA wind, which is at 6-h intervals.

accuracy that is unlikely to be achievable in the foreseeable future. In other words, we seek the upper bound in prediction using a perfect model under nearly perfect initial and boundary conditions following Lorenz (1996).

c. *Predictability metric*

The limit in predictability will be quantified in terms of relative magnitude between the reference and error spectral energy, $R(k)$ and $E(k)$, defined respectively as

$$R(k) = \sum_{k_x^2+k_y^2=k^2} (\hat{x})^2_{k_x,k_y} \qquad (1)$$

and

$$E(k) = \sum_{k_x^2+k_y^2=k^2} \frac{1}{N-1} \sum_{i=1}^{N} \left(\hat{x'}_i\right)^2_{k_x,k_y}, \qquad (2)$$

where x denotes the variable in consideration, $\overline{x} = (1/N)\sum_{i=1}^{N} x_i$ is the ensemble mean, $x'_i = x_i - \overline{x}$ is the ensemble perturbation, subscript $i = 1, 2, \ldots, N$ indexes the ensemble member, the hat denotes the Fourier transformation in two horizontal dimensions, and the subscripts k_x and k_y are the zonal and meridional wavenumbers, respectively. Following Bei and Zhang (2014), the reference and error energy are decomposed into spectral components (i.e., a function of global wavenumber k) and calculated separately for each model variable to demonstrate the scale and variable dependency in predictability. The variables of interest in this study are the u- and v-component winds, temperature, specific humidity, and precipitation. For the sake of simplicity, the u and v winds are combined as kinetic energy (KE), that is, $(1/2)(u^2 + v^2)$. The reference and error KE are calculated by first evaluating (1) and (2) for u and v and then taking their average.

Bei and Zhang (2014) used only one perturbed simulation and its difference with the unperturbed (control) simulation to measure the error energy. Only one realization of forecast error was available; therefore, the predictability estimate was less robust. More ideally, one can use an ensemble to sample the forecast error and

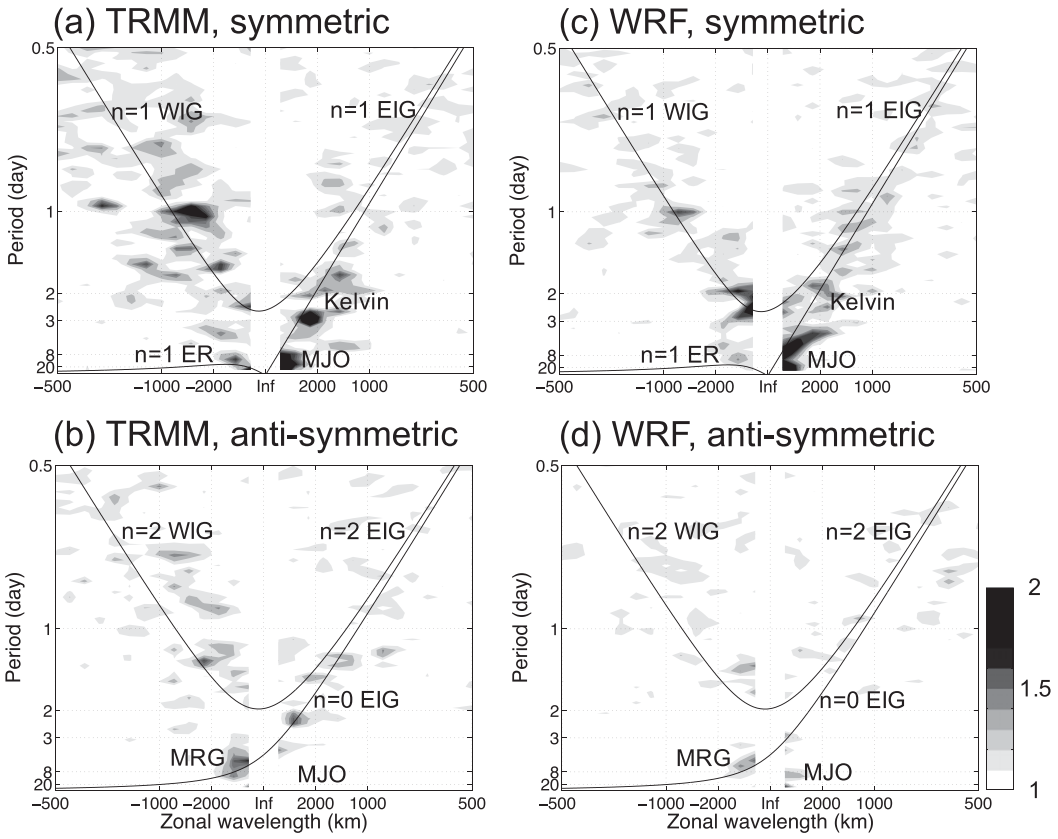

FIG. 3. Wheeler–Kiladis space–time spectra of precipitation from (a),(b) TRMM observation and (c),(d) WRF control simulation averaged over 15°S–15°N that is (a),(c) symmetric and (b),(d) antisymmetric about the equator. Signal strengths from 1.1 to 2 are shown (shading). The solid curves correspond to dispersion relations for dry equatorial waves with equivalent depth of 15 m. The zonal wavenumber and time frequency are labeled with corresponding zonal wavelength and time period, respectively; positive (negative) wavelength indicates eastward (westward)-propagating signals.

provide a much more robust estimate for predictability. In their predictability study on tropical cyclone intensity, Judt et al. (2016) defined an error energy as the averaged squared differences between two members from a 20-member ensemble, and the reference energy was defined as the averaged energy from each member. The predictability limit was defined as the forecast time at which error saturates; that is, the error energy becomes close enough to the reference energy. One caveat of this predictability limit definition is that the error growth usually slows down as it approaches saturation so that the exact saturation time is difficult to evaluate because of this asymptotic behavior.

In this study, a slightly different definition is used. The error energy (noise) is defined as the ensemble variance, and the reference energy (signal) is defined as the energy associated with the ensemble mean. As errors grow, the small-scale reference energy from the ensemble mean will decrease because of the smoothing among ensemble members. The predictability limit is defined as the forecast time at which error energy reaches and exceeds the reference energy (signal-to-noise ratio drops below 1).

3. Overview of the control simulation

The control simulation conducted in this study is mostly consistent with the control experiment results from Wang et al. (2015) except that the simulation starts from a later time and analysis nudging is not performed. The active MJO phase features the eastward propagation of large-scale organized convection and precipitation. Figure 1 compares the 5-day accumulated precipitation from the control simulation to the Tropical Rainfall Measuring Mission (TRMM) observations. During the simulated period, the precipitation center moves across the Indian Ocean (phases 1–3) and to the Maritime Continent (phases 4 and 5). The propagation of the MJO is not at a constant speed. Phase 2 takes much longer (10 days) than the following phases.

Consistent with Wang et al. (2015), the eastward propagation of the simulated precipitation agrees with the observation as shown in the Hovmöller diagrams in Fig. 2. At 850 hPa, westerlies (easterlies) are found west (east) of the precipitation center, which is the typical large-scale MJO flow pattern.

At smaller scales, the simulated precipitation shows IG wave signals over the Maritime Continent (90°–120°E). The propagation direction of these IG waves follows the prevailing zonal wind, that is, WIG waves in easterly wind and vice versa. At least some of these waves and precipitation patterns over the Maritime Continent are likely forced by the thermal diurnal cycles associated with the landmass (Mapes et al. 2003; Love et al. 2011). The precipitation over the Indian Ocean (50°–90°E) is organized into several 2-day episodes that are modulated by the phase of the MJO and several episodes of westward-propagating equatorial Rossby waves and eastward-propagating equatorial Kelvin waves (hereafter referred to as Rossby and Kelvin waves for simplicity). The model simulation of these finer-scale features is less accurate than the MJO signal itself as compared to the observations. There are generally mismatches in timing of the IG waves over the Indian Ocean.

However, the model simulation has a relatively good representation of the spectral modes of the multiscale CCEWs. Figure 3 compares the Wheeler and Kiladis (1999) space–time spectra (WK spectrum) of precipitation between the observation and the control simulation. Compared to the TRMM observation, the WRF simulation captures most of the CCEW modes although with errors in their signal strengths. The zonal wavelengths and time periods of the simulated waves agree with the observation except that Kelvin waves are propagating more slowly and the large-scale eastward-propagating IG (EIG) waves are missing the 2.5-day period in the simulation. The signal strengths of diurnal WIG, MRG, and Rossby waves are weaker in the simulation than in the observation, while Kelvin wave and MJO signal strengths are comparable to the observation. The large-scale 2-day WIG wave signals are simulated stronger than the observation. The WK spectra are calculated for a single MJO active phase during the simulated 1-month period, which is a relatively short sample size. Therefore, the large-scale low-frequency wave signals are expected to have some errors due to sampling noises. The errors in model and the specified initial and boundary conditions also cause the simulated WK spectra to differ from observation. Despite these discrepancies, the WRF simulation provides a reasonable representation of the observed CCEW and well serves the need as a control simulation.

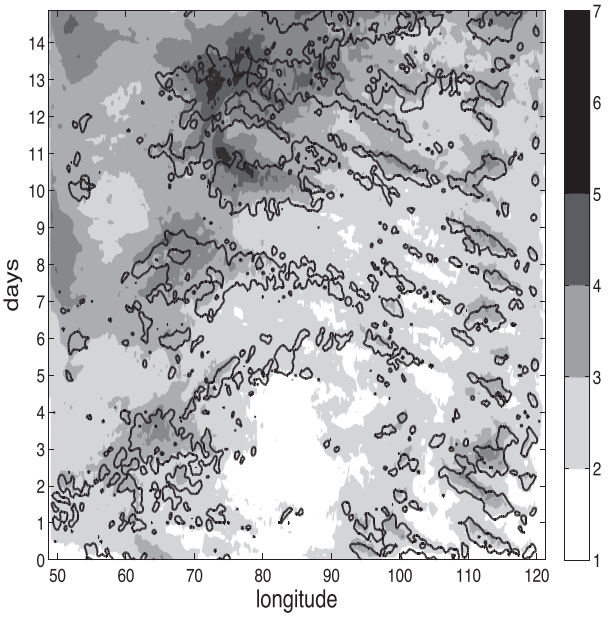

FIG. 4. Longitude–time plot of RM-DTE ($m\,s^{-1}$; shading) at 850 hPa and the precipitation from the control simulation (black contour of 15 mm day^{-1}) averaged over 5°S–5°N. The RM-DTE is the square root of ensemble-averaged DTE between the perturbed ensemble simulations and the control simulation from 18 Oct to 2 Nov (shown as t = 0–15 days).

4. Limit of practical predictability

To estimate the practical predictability (prediction skill) of the tropical multiscale weather and CCEWs, the error growth during the first ensemble simulation is investigated in this section. Figure 4 shows the longitude–time Hovmöller diagram of root-mean difference total energy [RM-DTE; as defined in Melhauser and Zhang (2012)], which is a combined measure of errors in horizontal winds and temperature. As forecast time progresses, the overall error increases because of the realistic uncertainties from the LBC. Larger RM-DTE is located near the region of stronger precipitation. There are apparent westward-propagating streaks of RM-DTE that are related to the CCEWs over the entire domain. The errors associated with the IG waves over the Maritime Continent have diurnal maxima following the peak precipitation, and there is no obvious trend during the 2-week period. On the other hand, the three successive moist phases of Kelvin waves over the Indian Ocean has increasingly larger errors. Such error growth behavior indicates a flow dependency in predictability that is more limited in the areas of precipitative systems.

Figure 5 shows the spectra of reference and error energy, $E(k)$ and $R(k)$, for KE, temperature, specific humidity, and precipitation. Let $l = k^{-1}$ be the horizontal wavelength; the spectra are plotted as a function

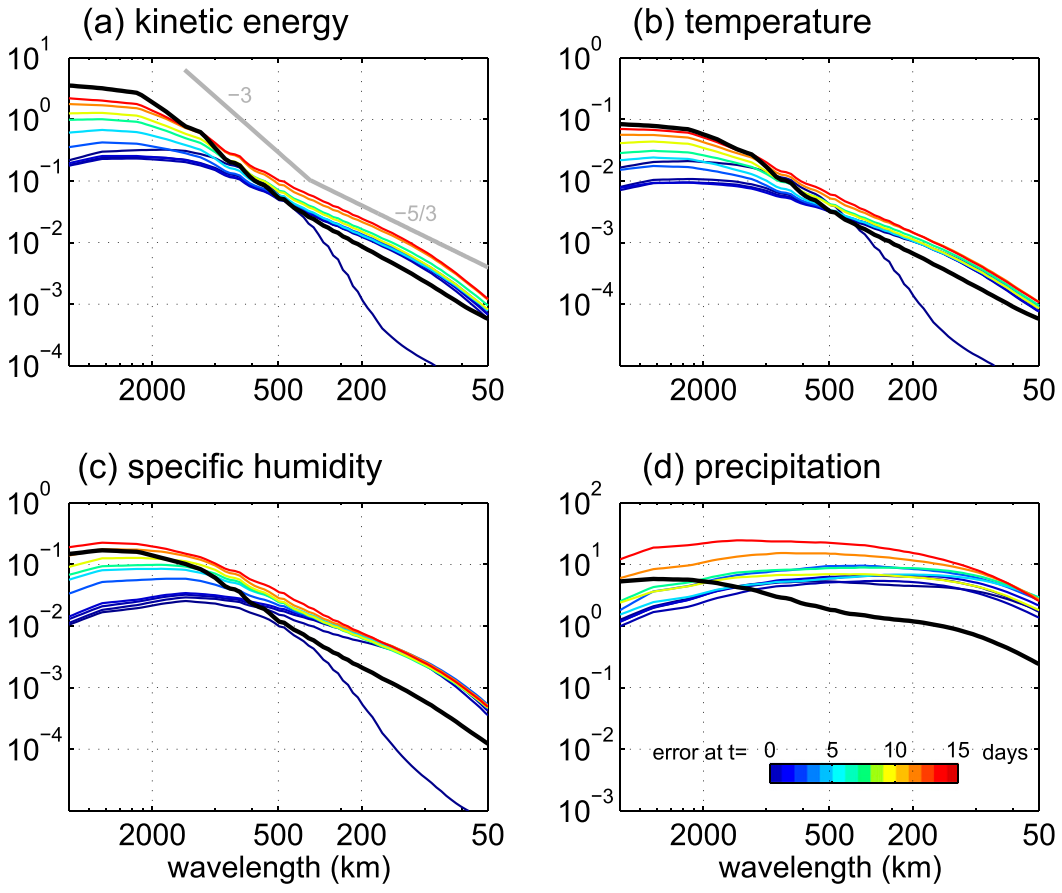

FIG. 5. Reference energy spectra $R(k)$ averaged over the 15 days (black lines) and error energy spectra $E(k)$ (color coded with simulation time t = 0–15 days) for (a) kinetic energy, (b) temperature, (c) specific humidity, and (d) precipitation. The shown spectrum is averaged over the vertical levels.

of k but labeled with its corresponding l values. The time-averaged reference KE spectrum (black line in Fig. 5a) has a −5/3 slope at small scales and transitions to a steeper −3 slope at around l = 500 km toward larger scales. According to Lorenz (1969) and Rotunno and Snyder (2008), there will be a predictability limit for the small scales because of its shallower spectral slope. The temperature and humidity spectra (Figs. 5b,c) have a similar shape compared to the KE spectrum, while the precipitation spectrum (Fig. 5d) is much shallower. Error energy spectral evolution can be viewed from the colored lines with time progresses from blue to red. At t = 0, the initial error KE from the ECMWF analysis is about one order of magnitude smaller than the reference energy at large scales and becomes comparable with reference energy at intermediate scales around l = 500 km. The initial error is artificially too small at small scales, because the ECMWF analyses are archived at a relatively coarse resolution (32 km) and thus not fully resolving l < 200 km. The error growth is more or less linear at larger scales, while the small-scale error saturates almost immediately. At small scales, the error energy exceeds the time-averaged reference energy, indicating the loss of predictability. Compared to other variables, precipitation has a wider range of scales with lost predictability after several forecast days.

To further illustrate the time evolution of errors at different scales, the reference and error energy are averaged over three arbitrarily selected scale ranges: large (l > 2000 km), intermediate (200 < l < 2000 km), and small (l < 200 km), and their time series are shown in Fig. 6. The errors in KE, temperature, and humidity have similar multistage growth behavior as described in Zhang et al. (2007). Small-scale errors grow the fastest in the first 12 h, and then after saturation, they stay at relatively the same level. Large- and intermediate-scale errors grow slowly during the whole simulation period, and the large-scale error never reached reference energy for KE. The predictability limit not only depends on the rate of error growth but is also complicated by the variations in reference energy. For temperature, the reference energy has a clear diurnal cycle at both large and

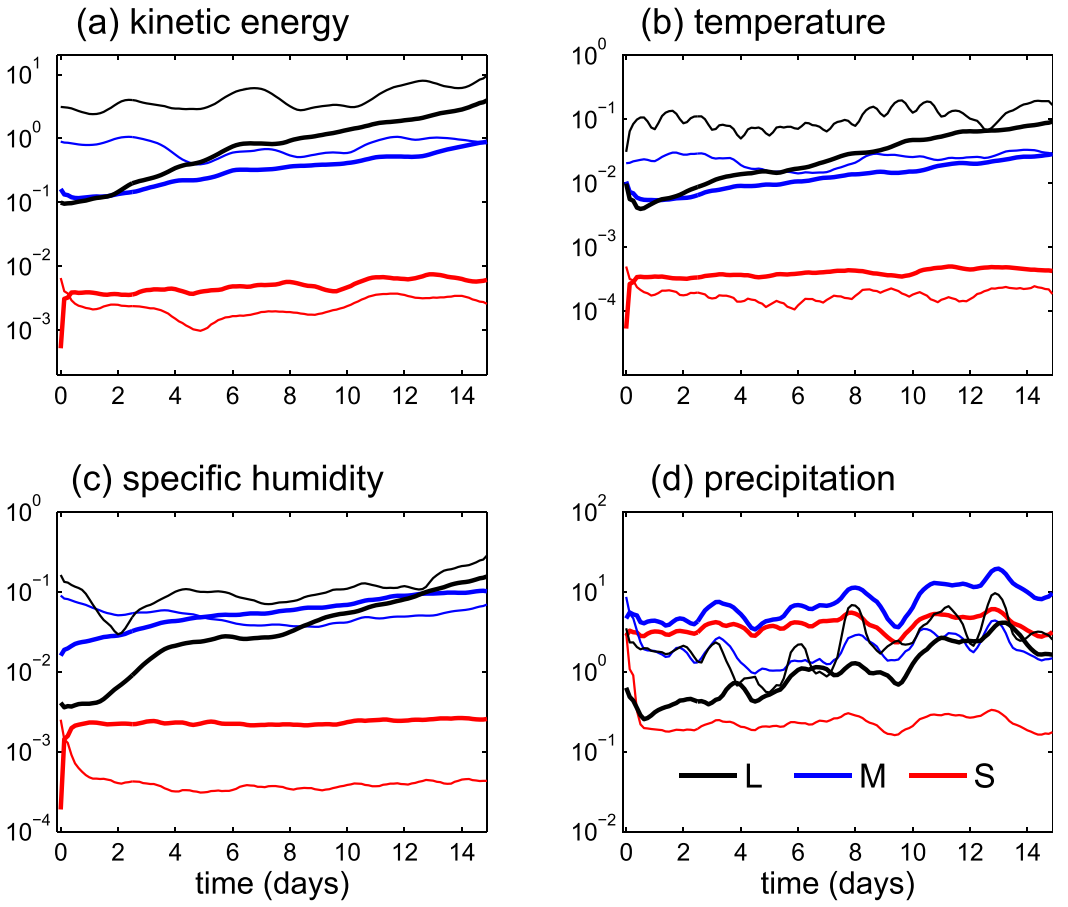

FIG. 6. Time series of spectral energy averaged at large (L; $l > 2000$ km; black), intermediate (M; $200 < l < 2000$ km; blue), and small (S; $l < 200$ km; red) scales for (a) kinetic energy, (b) temperature, (c) specific humidity, and (d) precipitation. The thick lines show the error energy, while thin lines show the reference energy.

small scales. The large-scale reference energy also appears to be modulated by the low-frequency waves; the humidity reference energy has three minima that are associated with the precipitation episodes over the Indian Ocean. For precipitation, the small- and intermediate-scale error energy exceeds their corresponding reference energy very early in the simulation, and the large-scale error energy is comparable to the reference after 4 days of simulation, but the exact time for loss of predictability is uncertain because of the constantly varying reference energy.

Figure 7 plots the estimated practical predictability limits (thick lines) as a function of horizontal wavelength. At large scales, the KE and temperature have practical predictability limits up to 15 days, followed by the specific humidity, which has a limit of 8 days, and practical predictability of precipitation is limited to only 3 days. The predictability of all variables dropped significantly across the intermediate scale. The practical predictability is limited to less than 12 h for KE, temperature, and specific humidity for scales $l < 200$ km and $l < 800$ km for precipitation.

5. Limit of intrinsic predictability

In this section, the intrinsic predictability limit is identified by investigating the second ensemble simulation with IC and LBC error energy reduced to 1%, a level of accuracy that is unlikely to be attainable in the foreseeable future. Figure 8 shows the time series of error energy of this new ensemble (red) for KE and precipitation at three scales and compares their error evolution to the original ensemble with 100% error (blue). When error energy is reduced to 1%, the large- and intermediate-scale error KE (Figs. 8a,b) still grows at a similar rate as the 100% error case during most of the simulation period, although there is some indication of increased error growth rate during the first 3 days. By the end of simulation, error KE from the 1%-error case remains an order of magnitude lower than that from the

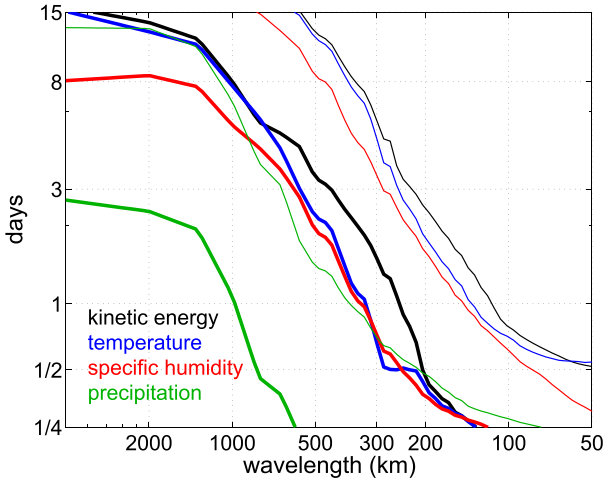

FIG. 7. Predictability limits for kinetic energy (black), temperature (blue), specific humidity (red), and precipitation (green) plotted as a function of zonal wavenumber (labeled as wavelength). Thick (thin) lines are practical (intrinsic) predictability limits. The limits are defined as the time it takes for the error energy (100% error for practical limit and 1% error for intrinsic limit) to reach reference energy. The limits are calculated for each member, and the ensemble average is plotted. Smoothing is applied across the wavelength to remove some noise for better visualization.

100%-error case. This indicates that the intrinsic predictability for these scales is likely to be achievable beyond the 15-day simulation period, since the predictability horizon can be extended by reducing the IC and LBC errors.

On the other hand, the small-scale error KE (Fig. 8c) grows much more rapidly and the reduced error only delays the loss of predictability by about 1 day. This behavior is as expected according to Rotunno and Snyder (2008) because of the −5/3 power law of small-scale KE. The intermediate-scale KE error growth rate is higher at the beginning of the simulation, because part of the intermediate-scale range has a shallower KE spectrum ($200 < l < 500$ km). The temperature and humidity error energy results for the 1%-error case are similar to KE (not shown), and precipitation (Figs. 8d–f) also displays similar behavior, but its range of scales that have limited predictability is much wider than other variables. The intrinsic predictability limits are also plotted as thin lines in Fig. 7 as a function of horizontal wavenumber. For the −5/3 power-law range ($l <$ 500 km), theories predict that predictability will be limited. The results are consistent with the theory that reducing the IC and LBC error perturbations to 10% does not increase the predictability limit 10 times. The intrinsic predictability limit for KE is about 10 days at $l = 500$ km and decreases to <1 day at small scales. The same predictability limit is true for other variables such as temperature and humidity but not for precipitation, which has more limited intrinsic predictability.

For regional models, the specification of LBC is nontrivial for the accuracy of simulation. To evaluate the relative importance of IC and LBC, an extra set of ensemble simulations are conducted with perturbations (from 100% error) only added to the IC, and the results are plotted in Fig. 8 as gray lines (IC error only). For large- and intermediate-scale KE, the LBC error contributes a lot to the overall error growth; without LBC error, the error energy remains at a similar IC error level throughout the simulation. However, for small-scale KE, a correct LBC does not help to reduce the initial error growth; it only slightly reduces errors later in the simulation when they are already saturated. For precipitation, the large-scale error energy is reduced by specifying a correct LBC, while the intermediate- and small-scale errors are not significantly reduced before saturation. The intermediate-scale precipitation error is only occasionally lowered with the correct LBC, indicating a mixed influence from the boundary and local regions.

Similar to the definition of error doubling time (Lorenz 1969), an "error growth time" is defined as the time in which the initial error energy grows two orders of magnitude (from 1% to 100% initial error energy). Figure 9 plots the error growth time as a function of the horizontal wavenumber. For $l > 500$ km, the error growth time exceeds 15 days for KE and temperature and ~10 days for humidity. The error growth rate rapidly increases as l decreases from 500 to 100 km; for $l <$ 100 km, the error growth time is well below 6 h. The precipitation error growth rate is much higher than other variables for the large and intermediate scales. However, its error growth rate increases more smoothly across scales, unlike other variables that have a rapid growth-rate boost within a narrow scale band.

6. Predictability of CCEWs at different scales

In the previous sections, the practical and intrinsic predictability limits are estimated for different model variables and for different spatial scales. To identify the underlying processes for the error growth at different spatial and temporal scales, a Wheeler–Kiladis space–time spectral analysis is conducted in this section to extract CCEWs from the simulation and study the predictability associated with each wave mode.

Figure 10 shows the WK spectra for precipitation from the control simulation. Both the zonal wavenumber and time frequency axes are shown in log scale. The spatial scale is again separated into large (L), intermediate (M), and small (S) scales similar to previous sections; the specified temporal- and spatial-scale

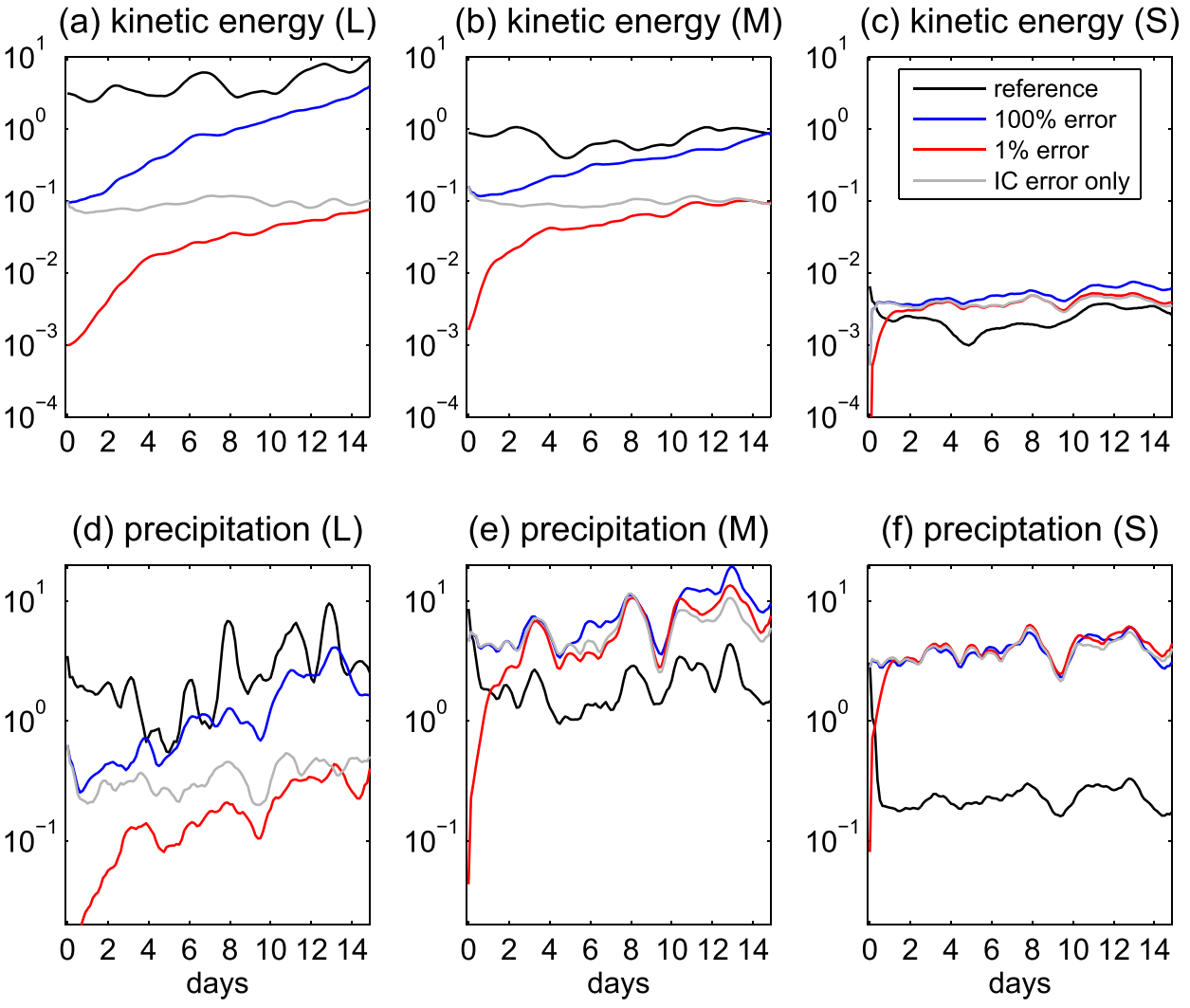

FIG. 8. Time series of spectral error energy integrated within (a),(d) L, (b),(e) M, and (c),(f) S scales for (a)–(c) kinetic energy and (d)–(f) precipitation. The reference error energy is shown as black lines, the blue (red) lines show the error energy from the 100% (1%)-error case, and the gray lines show the case with errors only in the initial condition.

windows for the CCEWs are indicated with black boxes. Along with the MJO signal, the Rossby ($n = 1$ ER), Kelvin, MRG, 2-day WIG ($n = 1$ WIG_L), and EIG ($n = 0$ EIG_L) waves all reside in the large scale. At intermediate scales, the $n = 1$ IG waves (WIG_M and EIG_M) with diurnal to semidiurnal periods are the dominant wave modes. The small scale has no clearly identifiable wave signals. Precipitation signals related to small-scale moist convection spread throughout the small-scale spectrum, and according to the previous sections, its predictability is intrinsically limited to <1 day.

A space–time bandpass filter is applied to the precipitation field to extract each wave mode according to its period and wavelength window as shown in Fig. 10. Since the perturbed ensemble forecast is performed only for a shorter 15-day period, the control simulation is used to fill in the missing days before filtering. Figures 11a–e show longitude–time plots for the filtered precipitation associated with large-scale waves. Spaghetti plots of a selected precipitation contour (black) among members from the first ensemble (100% error) are shown in Figs. 11f–j, and they are compared to the 1%-error cases in Figs. 11k–o. For the ensemble with 100% error sampled from the ECMWF forecasts, the precipitation contours diverge and become out of phase. However, when the error energy is reduced to 1%, the contours remain in phase among members throughout the whole simulation. The same analysis is performed for the intermediate-scale IG waves, and results are shown in Fig. 12. In contrast to large-scale-wave results, the error reduction does not bring the contours in phase and large displacement errors still

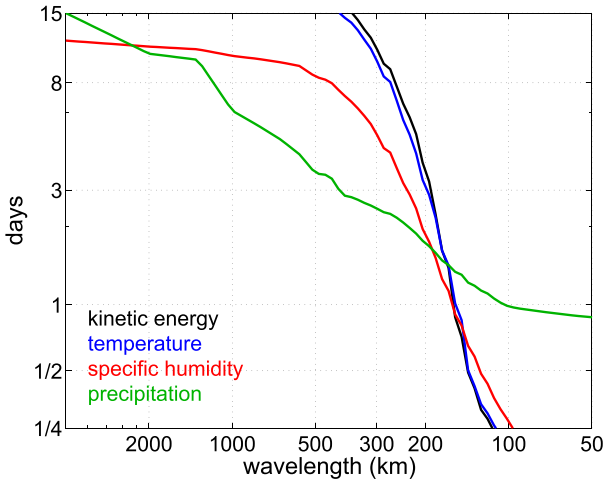

FIG. 9. Error growth time (days) plotted as a function of zonal wavenumber (labeled as wavelength) for kinetic energy (black), temperature (blue), specific humidity (red), and precipitation (green). The error growth time is defined as the time it takes for 1% initial error to grow and reach 100% initial error. The growth time is calculated for each member, and the ensemble average is plotted.

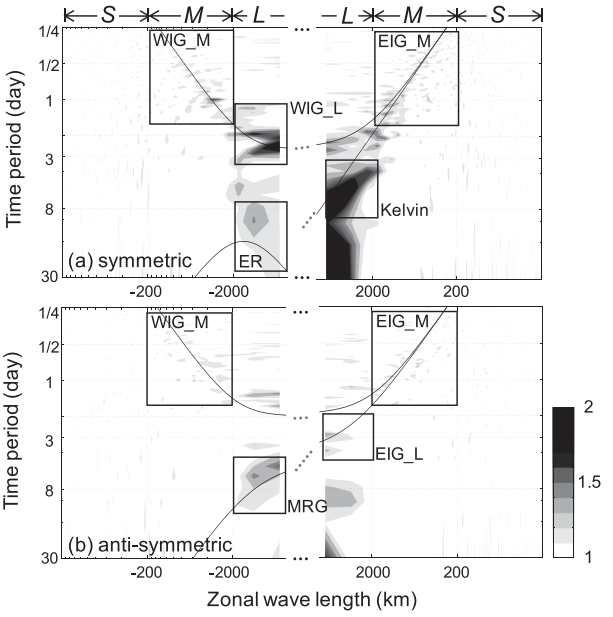

FIG. 10. As in Figs. 3c and 3d, but for zonal wavenumber and time frequency shown in log scale. Space–time filtering windows are shown as black boxes for ER wave, Kelvin wave, MRG wave, $n = 1$ WIG wave at intermediate scale (WIG_M) and at large scale (WIG_L), $n = 0$ EIG at large scale (EIG_L), and $n = 1$ EIG at intermediate scale (EIG_M).

exist for intermediate-scale waves. These results agree with the findings from the previous section that the estimated large-scale predictability for precipitation can potentially be extended from 3 to ~15 days if errors are reduced to 1%, while for intermediate scales, its predictability remains intrinsically limited (Fig. 7).

Table 1 lists the averaged pattern correlations between perturbed and unperturbed simulations as a more quantitative measure of CCEW phase errors. A correlation of 1 indicates that two waves are perfectly in phase, while zero correlation indicates two waves completely out of phase. For precipitation, the large-scale CCEWs all show that a significant improvement in wave phase (from ~0.6 to ~0.8 correlation) is possible, which is contrasted by the intermediate-scale IG waves that stay out of phase (correlation <0.3) even with reduced error. For other variables, results from the previous section show that the practical predictability for KE, temperature, and humidity is much less limited than precipitation at large and intermediate scales. Therefore, the zonal wind, temperature, and humidity phases associated with Rossby, Kelvin, and MRG waves can potentially be improved to almost perfect (correlation >0.9) with reduced error. The intermediate-scale predictability for zonal wind, temperature, and humidity is more limited but less so than precipitation.

7. Concluding remarks

In this study, the October 2011 MJO active phase is simulated using the WRF Model with similar configuration as Wang et al. (2015). The control simulation is initialized with ERA-Interim data. The model faithfully reproduced most of the large-scale features of the MJO and CCEWs. We conducted 20 perturbed simulations for the 15-day period from 18 October to 2 November to estimate the practical predictability of the multiscale tropical weather. The IC and LBC perturbations are sampled from the ECMWF global ensemble forecasts from the TIGGE archive. Predictability limit is defined as the time in which error energy (ensemble variance) reaches/exceeds the reference energy (energy associated with the ensemble-mean field). Intrinsic predictability is identified by another set of perturbed simulations with the IC and LBC error energy reduced to 1%. Two-dimensional spectral decomposition is applied to the error and reference energy to reveal the horizontal-scale dependency in predictability. The predictability limits are calculated separately for kinetic energy, temperature, specific humidity, and precipitation at each scale. Findings from this study are summarized as follows:

1) The practical predictability is scale and variable dependent. For large-scale ($l > 2000$ km) horizontal winds and temperature, the practical predictability limit is ~15 days, and for humidity, the limit is ~8 days. The predictability rapidly drops across the

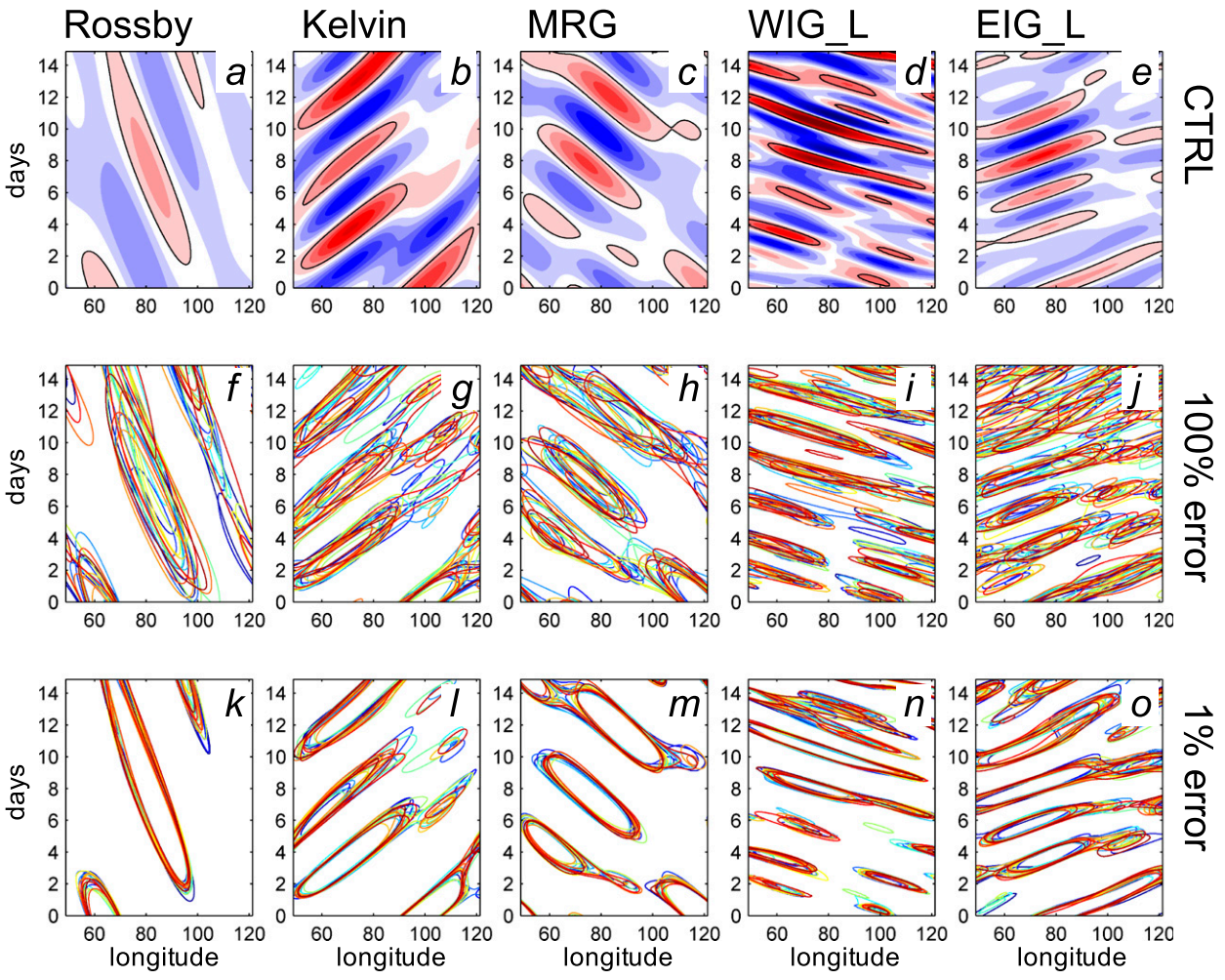

FIG. 11. (a)–(e) Longitude–time plots of precipitation (color shading every 1 mm day^{-1} from −10 to 10 mm day^{-1}; zero shown in white) filtered for (a) Rossby, (b) Kelvin, (c) MRG, (d) WIG_L, and (e) EIG_L waves and averaged over 0°–5°N. (f)–(j) Spaghetti plots of the contours highlighted in black in (a)–(e); each color corresponds to a member from the perturbed ensemble simulation (100%-error case). (k)–(o) As in (f)–(j), respectively, but for the ensemble simulation with error energy reduced to 1%.

intermediate scale ($200 < l < 2000$ km), and for small scales ($l < 200$ km), their practical predictability is limited to <12 h. Precipitation has more limited predictability than other variables; its large-scale practical predictability limit is only 3 days and drops to <12 h for the smaller scales.

2) Intrinsic predictability limits for horizontal winds, temperature, and humidity are >10 days for scales larger than 500 km. At these larger scales, the practical predictability horizon can be well extended by reducing errors in IC and LBC. However, for scales smaller than 500 km, the intrinsic predictability limit decreases; at <100-km scales, the limit is <1 day, which is likely related to a shallower −5/3 power law in the KE spectrum. For precipitation, a wider range of its smaller scales has intrinsically limited predictability compared to other variables.
3) Error growth rate is low at large scales and high at small scales; the increase takes place in a very narrow scale range (100–500 km) for horizontal winds, temperature, and humidity. On the other hand, precipitation error growth rate increases more smoothly across scales.
4) Large-scale CCEWs (i.e., Rossby, Kelvin, MRG, and the 2-day IG waves) have a predictability that can be potentially improved by reducing the IC and LBC errors. With errors reduced to 1%, the zonal wind, temperature, and humidity associated with large-scale waves can be improved to almost perfectly in phase. However, for the intermediate scale, the diurnal and semidiurnal IG waves have a predictability that is more intrinsically limited.

The current findings encourage the future development in data assimilation and modeling systems to

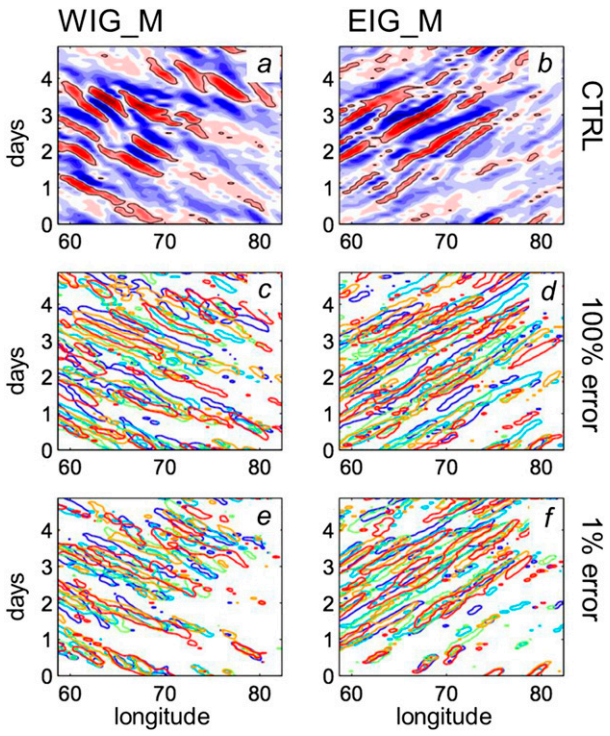

FIG. 12. As in Fig. 11, but for the two intermediate-scale waves, WIG_M and EIG_M. Only five members are shown in the spaghetti plots, and the longitude–time plots are zoomed in on 60°–80°E and the first 5 days of the simulation.

TABLE 1. Averaged pattern correlation between member (perturbed run) and the control (unperturbed run) for zonal wind, temperature, specific humidity, and precipitation associated with each CCEW mode. The improvement in pattern correlation from the 100% error case to the 1% error case is indicated by an arrow.

CCEW mode	Zonal wind	Temperature	Specific humidity	Precipitation
Rossby	0.84→0.99	0.85→0.99	0.72→0.97	0.75→0.88
Kelvin	0.77→0.97	0.82→0.97	0.67→0.92	0.65→0.85
MRG	0.75→0.95	0.64→0.94	0.65→0.94	0.64→0.86
WIG_L	0.51→0.86	0.51→0.86	0.46→0.81	0.45→0.74
EIG_L	0.51→0.85	0.64→0.92	0.49→0.83	0.46→0.70
WIG_M	0.27→0.43	0.38→0.50	0.27→0.44	0.17→0.28
EIG_M	0.16→0.27	0.33→0.45	0.17→0.32	0.09→0.17

further improve the predictability of CCEWs. However, the authors would like to point out some caveats in interpreting the results in this paper. The convection-permitting WRF Model, although providing a reasonable representation of CCEWs, is still not perfect. In this study, only the uncertainties from model IC and LBC are accounted for when estimating practical predictability. While the IC and LBC uncertainties are sampled from realistic forecast errors, the estimated practical predictability may potentially differ from those estimated from other modeling systems that account for additional error sources (e.g., model dynamics, physics parameterizations, and low-boundary-condition forcings). The predictability estimates from the MJO active phase event in this study may also differ from those estimated for other events.

The current study only simulates a 15-day period within an MJO active phase, which is not long enough to estimate the predictability of MJO itself. In previous MJO predictability studies using global model simulations, the practical predictability estimates range from 15 to 45 days, depending on the models and diagnostics used (Gottschalck et al. 2010; Vitart and Molteni 2010; Neena et al. 2014b; Hamill and Kiladis 2014). The MJO predictability metric is usually based on the real-time multivariate MJO (RMM) index (Wheeler and Hendon 2004), which captures more of the large-scale features of the MJO signal. Ling et al. (2014) suggested that, when finer-scale local features are included, the estimated predictability becomes more limited than when using a global measure. The predictability of MJO is also found to be dependent on its phase (Waliser et al. 2003; Nasuno 2013; Neena et al. 2014a,b). While the active phase of the MJO has better predictability, the models have difficulty in accurately predicting the timing of convection onset during its suppressed phase. As an extension of these global model MJO predictability studies, the current study provides a comprehensive predictability estimate for the multiscale CCEWs during an MJO active phase. How the predictability estimates change for a suppressed MJO phase may be a future research topic.

The selection of MJO diagnostics is also nontrivial in predictability studies. Waliser et al. (2009) proposed several candidate MJO diagnostics that can capture more small-scale details of MJO than traditional ones. Results in this paper show that predictability is variable dependent. Therefore, process-oriented diagnostics (Kim et al. 2014) that targets the tropospheric moisture or even precipitation may result in very different predictability estimates compared to just using dynamic variables. A longer regional simulation with convection-permitting resolution may be the next step to facilitate a comprehensive predictability study that compares different diagnostics.

Acknowledgments. This research was supported by NSF Grant AGS-1305798. Yue Ying was also sponsored by the China Scholarship Council (CSC) visitor program. Computing is performed at the Texas Advanced Computing Center (TACC). All model output used in the study can be freely accessed at the data archive facility of TACC. The authors also appreciate the anonymous comments from three reviewers that improved an earlier version of this paper.

REFERENCES

Bei, N., and F. Zhang, 2007: Impacts of initial condition errors on mesoscale predictability of heavy precipitation along the Mei-Yu front of China. *Quart. J. Roy. Meteor. Soc.*, **133**, 83–99, doi:10.1002/qj.20.

——, and ——, 2014: Mesoscale predictability of moist baroclinic waves: Variable and scale-dependent error growth. *Adv. Atmos. Sci.*, **31**, 995–1008, doi:10.1007/s00376-014-3191-7.

Chen, F., and J. Dudhia, 2001: Coupling an advanced land surface hydrology model with the Penn State–NCAR MM5 modeling system. Part I: Model implementation and sensitivity. *Mon. Wea. Rev.*, **129**, 569–585, doi:10.1175/1520-0493(2001)129<0569:CAALSH>2.0.CO;2.

Collins, W. D., and Coauthors, 2004: Description of the NCAR Community Atmosphere Model (CAM 3.0). NCAR Tech. Note NCAR/TN-464+STR, 214 pp.

Dee, D. P., and Coauthors, 2011: The ERA-Interim reanalysis: Configuration and performance of the data assimilation system. *Quart. J. Roy. Meteor. Soc.*, **137**, 553–597, doi:10.1002/qj.828.

Dickinson, M., and J. Molinari, 2002: Mixed Rossby–gravity waves and western Pacific tropical cyclogenesis. Part I: Synoptic evolution. *J. Atmos. Sci.*, **59**, 2183–2196, doi:10.1175/1520-0469(2002)059<2183:MRGWAW>2.0.CO;2.

Dunkerton, T. J., and F. X. Crum, 1995: Eastward propagating ~2- to 15-day equatorial convection and its relation to the tropical intraseasonal oscillation. *J. Geophys. Res.*, **100**, 25 781–25 790, doi:10.1029/95JD02678.

Gottschalck, J., and Coauthors, 2010: A framework for assessing operational Madden–Julian oscillation forecasts: A CLIVAR MJO Working Group project. *Bull. Amer. Meteor. Soc.*, **91**, 1247–1258, doi:10.1175/2010BAMS2816.1.

Haertel, P. T., and G. N. Kiladis, 2004: Dynamics of 2-day equatorial waves. *J. Atmos. Sci.*, **61**, 2707–2721, doi:10.1175/JAS3352.1.

Hamill, T. M., and G. N. Kiladis, 2014: Skill of the MJO and Northern Hemisphere blocking in GEFS medium-range reforecasts. *Mon. Wea. Rev.*, **142**, 868–885, doi:10.1175/MWR-D-13-00199.1.

Hong, S.-Y., Y. Noh, and J. Dudhia, 2006: A new vertical diffusion package with an explicit treatment of entrainment processes. *Mon. Wea. Rev.*, **134**, 2318–2341, doi:10.1175/MWR3199.1.

Johnson, R. H., and P. E. Ciesielski, 2013: Structure and properties of Madden–Julian oscillations deduced from DYNAMO sounding arrays. *J. Atmos. Sci.*, **70**, 3157–3179, doi:10.1175/JAS-D-13-065.1.

Judt, F., S. S. Chen, and J. Berner, 2016: Predictability of tropical cyclone intensity: Scale-dependent forecast error growth in high-resolution stochastic kinetic-energy backscatter ensembles. *Quart. J. Roy. Meteor. Soc.*, **142**, 43–57, doi:10.1002/qj.2626.

Kiladis, G. N., M. C. Wheeler, P. T. Haertel, K. H. Straub, and P. E. Roundy, 2009: Convectively coupled equatorial waves. *Rev. Geophys.*, **47**, RG2003, doi:10.1029/2008RG000266.

Kim, D., and Coauthors, 2014: Process-oriented MJO simulation diagnostic: Moisture sensitivity of simulated convection. *J. Climate*, **27**, 5379–5395, doi:10.1175/JCLI-D-13-00497.1.

Lim, K.-S. S., and S.-Y. Hong, 2010: Development of an effective double-moment cloud microphysics scheme with prognostic cloud condensation nuclei (CCN) for weather and climate models. *Mon. Wea. Rev.*, **138**, 1587–1612, doi:10.1175/2009MWR2968.1.

Ling, J., P. Bauer, P. Bechtold, A. Beljaars, R. Forbes, F. Vitart, and C. Zhang, 2014: Global versus local MJO forecast skill of the ECMWF model during DYNAMO. *Mon. Wea. Rev.*, **142**, 2228–2247, doi:10.1175/MWR-D-13-00292.1.

Lorenz, E. N., 1963: Deterministic nonperiodic flow. *J. Atmos. Sci.*, **20**, 130–141, doi:10.1175/1520-0469(1963)020<0130:DNF>2.0.CO;2.

——, 1969: Atmospheric predictability as revealed by naturally occurring analogues. *J. Atmos. Sci.*, **26**, 636–646, doi:10.1175/1520-0469(1969)26<636:APARBN>2.0.CO;2.

——, 1982: Atmospheric predictability experiments with a large numerical model. *Tellus*, **34**, 505–513, doi:10.3402/tellusa.v34i6.10836.

——, 1996: Predictability—A problem partly solved. *Proc. Seminar on Predictability*, Reading, United Kingdom, ECMWF, 1–18.

Love, B. S., A. J. Matthews, and G. M. S. Lister, 2011: The diurnal cycle of precipitation over the Maritime Continent in a high-resolution atmospheric model. *Quart. J. Roy. Meteor. Soc.*, **137**, 934–947, doi:10.1002/qj.809.

Madden, R. A., and P. R. Julian, 1971: Detection of a 40–50 day oscillation in the zonal wind in the tropical Pacific. *J. Atmos. Sci.*, **28**, 702–708, doi:10.1175/1520-0469(1971)028<0702:DOADOI>2.0.CO;2.

——, and ——, 1972: Description of global-scale circulation cells in the Tropics with a 40–50 day period. *J. Atmos. Sci.*, **29**, 1109–1123, doi:10.1175/1520-0469(1972)029<1109:DOGSCC>2.0.CO;2.

Mapes, B. E., T. T. Warner, and M. Xu, 2003: Diurnal patterns of rainfall in northwestern South America. Part III: Diurnal gravity waves and nocturnal convection offshore. *Mon. Wea. Rev.*, **131**, 830–844, doi:10.1175/1520-0493(2003)131<0830:DPORIN>2.0.CO;2.

——, S. Tulich, T. Nasuno, and M. Satoh, 2008: Predictability aspects of global aqua-planet simulations with explicit convection. *J. Meteor. Soc. Japan*, **86A**, 175–185, doi:10.2151/jmsj.86A.175.

Melhauser, C., and F. Zhang, 2012: Practical and intrinsic predictability of severe and convective weather at the mesoscales. *J. Atmos. Sci.*, **69**, 3350–3371, doi:10.1175/JAS-D-11-0315.1.

Miyakawa, T., M. Satoh, H. Miura, H. Tomita, H. Yashiro, A. T. Noda, and K. Yoneyama, 2014: Madden–Julian oscillation prediction skill of a new-generation global model demonstrated using a supercomputer. *Nat. Commun.*, **5**, 3769, doi:10.1038/ncomms4769.

Nakazawa, T., 1988: Tropical super clusters within intraseasonal variations over the western Pacific. *J. Meteor. Soc. Japan*, **66**, 823–836, doi:10.2151/jmsj1965.66.6_823.

Nasuno, T., 2013: Forecast skill of Madden-Julian oscillation events in a global nonhydrostatic model during the CINDY2011/DYNAMO observation period. *SOLA*, **9**, 69–73, https://doi.org/10.2151/sola.2013-016.

Neena, J. M., J. Y. Lee, D. Waliser, B. Wang, and X. Jiang, 2014a: Predictability of the Madden–Julian oscillation in the Intraseasonal Variability Hindcast Experiment (ISVHE). *J. Climate*, **27**, 4531–4543, doi:10.1175/JCLI-D-13-00624.1.

——, X. Jiang, D. Waliser, J. Y. Lee, and B. Wang, 2014b: Eastern Pacific intraseasonal variability: A predictability perspective. *J. Climate*, **27**, 8869–8883, doi:10.1175/JCLI-D-14-00336.1.

Reynolds, C. A., and P. J. Webster, 1994: Random error growth in NMC's global forecasts. *Mon. Wea. Rev.*, **122**, 1281–1305, doi:10.1175/1520-0493(1994)122<1281:REGING>2.0.CO;2.

Rotunno, R., and C. Snyder, 2008: A generalization of Lorenz's model for the predictability of flows with many scales of motion. *J. Atmos. Sci.*, **65**, 1063–1076, doi:10.1175/2007JAS2449.1.

Selz, T., and G. C. Craig, 2015: Upscale error growth in a high-resolution simulation of a summertime weather event over Europe. *Mon. Wea. Rev.*, **143**, 813–827, doi:10.1175/MWR-D-14-00140.1.

Skamarock, W. C., and Coauthors, 2008: A description of the Advanced Research WRF version 3. NCAR Tech. Note NCAR/TN-475+STR, 113 pp., http://dx.doi.org/10.5065/D68S4MVH.

Sun, Y. Q., and F. Zhang, 2016: Intrinsic versus practical limits of atmospheric predictability and the significance of the butterfly effect. *J. Atmos. Sci.*, **73**, 1419–1438, doi:10.1175/JAS-D-15-0142.1.

Takayabu, Y. N., and T. S. Nitta, 1993: 3-5 day-period disturbances coupled with convection over the tropical Pacific Ocean. *J. Meteor. Soc. Japan*, **71**, 221–246, doi:10.2151/jmsj1965.71.2_221.

Tao, D., and F. Zhang, 2015: Effects of vertical wind shear on the predictability of tropical cyclones: Practical versus intrinsic limit. *J. Adv. Model. Earth Syst.*, **7**, 1534–1553, doi:10.1002/2015MS000474.

Vitart, F., and F. Molteni, 2010: Simulation of the Madden–Julian oscillation and its teleconnections in the ECMWF forecast system. *Quart. J. Roy. Meteor. Soc.*, **136**, 842–855, doi:10.1002/qj.623.

Waliser, D. E., K. M. Lau, W. Stern, and C. Jones, 2003: Potential predictability of the Madden–Julian oscillation. *Bull. Amer. Meteor. Soc.*, **84**, 33–50, doi:10.1175/BAMS-84-1-33.

——, and Coauthors, 2009: MJO simulation diagnostics. *J. Climate*, **22**, 3006–3030, doi:10.1175/2008JCLI2731.1.

Wang, S., A. H. Sobel, F. Zhang, Y. Q. Sun, Y. Yue, and L. Zhou, 2015: Regional simulation of the October and November MJO events observed during the CINDY/DYNAMO field campaign at gray zone resolution. *J. Climate*, **28**, 2097–2119, doi:10.1175/JCLI-D-14-00294.1.

Wheeler, M. C., and G. N. Kiladis, 1999: Convectively coupled equatorial waves: Analysis of clouds and temperature in the wavenumber–frequency domain. *J. Atmos. Sci.*, **56**, 374–399, doi:10.1175/1520-0469(1999)056<0374:CCEWAO>2.0.CO;2.

——, and H. H. Hendon, 2004: An all-season real-time multivariate MJO index: Development of an index for monitoring and prediction. *Mon. Wea. Rev.*, **132**, 1917–1932, doi:10.1175/1520-0493(2004)132<1917:AARMMI>2.0.CO;2.

Yoneyama, K., C. Zhang, and C. N. Long, 2013: Tracking pulses of the Madden–Julian oscillation. *Bull. Amer. Meteor. Soc.*, **94**, 1871–1891, doi:10.1175/BAMS-D-12-00157.1.

Zeng, X., and A. Beljaars, 2005: A prognostic scheme of sea surface skin temperature for modeling and data assimilation. *Geophys. Res. Lett.*, **32**, L14605, doi:10.1029/2005GL023030.

Zhang, C., 2005: Madden-Julian oscillation. *Rev. Geophys.*, **43**, RG2003, https://doi.org/10.1029/2004RG000158.

——, J. Gottshalck, E. D. Maloney, M. W. Moncrieff, F. Vitart, D. E. Waliser, B. Wang, and M. C. Wheeler, 2013: Cracking the MJO nut. *Geophys. Res. Lett.*, **40**, 1223–1230, doi:10.1002/grl.50244.

Zhang, F., and J. A. Sippel, 2009: Effects of moist convection on hurricane predictability. *J. Atmos. Sci.*, **66**, 1944–1961, doi:10.1175/2009JAS2824.1.

——, C. Snyder, and R. Rotunno, 2002: Mesoscale predictability of the "surprise" 24–25 January 2000 snowstorm. *Mon. Wea. Rev.*, **130**, 1617–1632, doi:10.1175/1520-0493(2002)130<1617:MPOTSS>2.0.CO;2.

——, ——, and ——, 2003: Effects of moist convection on mesoscale predictability. *J. Atmos. Sci.*, **60**, 1173–1185, doi:10.1175/1520-0469(2003)060<1173:EOMCOM>2.0.CO;2.

——, A. M. Odins, and J. W. Nielsen-Gammon, 2006: Mesoscale predictability of an extreme warm-season precipitation event. *Wea. Forecasting*, **21**, 149–166, doi:10.1175/WAF909.1.

——, N. Bei, R. Rotunno, C. Snyder, and C. C. Epifanio, 2007: Mesoscale predictability of moist baroclinic waves: Convection-permitting experiments and multistage error growth dynamics. *J. Atmos. Sci.*, **64**, 3579–3594, doi:10.1175/JAS4028.1.

——, S. Talaphdar, and S. Wang, 2017: The role of global circumnavigating mode in the MJO initiation and propagation. *J. Geophys. Res. Atmos.*, **122**, 5837–5856, https://doi.org/10.1002/2016JD025665.

Zhang, Y., F. Zhang, D. J. Stensrud, and Z. Meng, 2016: Intrinsic predictability of the 20 May 2013 tornadic thunderstorm event in Oklahoma at storm scales. *Mon. Wea. Rev.*, **144**, 1273–1298, doi:10.1175/MWR-D-15-0105.1.